

Erosion Control for Highly Efficient Propellers Using a Boundary Element Method Coupled With a Bubble Dynamics Model

Stephan Berger*, Yasaman Mirsadraee, Keun Woo Shin, Rasmus Møller Bering

MAN Energy Solutions, Aft Ship & Propeller, MAN PrimeServ Four-Stroke Denmark, Frederikshavn, Denmark

ABSTRACT

A combined approach for controlling the erosion risk of marine propellers is introduced in this paper. By means of a BEM code, the propeller flow in terms of velocity and pressure distribution is simulated. Cavitation bubbles are released at the leading edge of the propeller, and their dynamical behavior is modeled by the Rayleigh-Plesset Equation. These bubbles are interpreted as an idealized form of propeller cavitation, which can highlight unfavorable pressure distributions as well as crucial details in the blade design that could potentially cause erosion. For this purpose, the bubbles are traced when passing the blade surface, and their growth and shrinkage is evaluated. Inspired by the so-called Discrete Bubble Method, the acoustic pressure radiated by a collapsing bubble is related to a potential loss of material, i.e. the erosion risk. The influence of the ship's wake field can be taken into account by the method, and it turns out that the wake field can have a big influence on the erosion risk. This paper addresses the theoretical framework of the method and reports on its implementation using DTU's panel code ESPPRO. The newly developed tool is tested for two propeller designs and their respective design variants. Results obtained by the tool are compared to results of well-established DES erosion analysis.

Keywords

Propeller Cavitation & Erosion, Bubble Dynamics, Boundary Element Method

1 INTRODUCTION

When designing a propeller, engineers must find an optimal compromise between propulsive efficiency and cavitation behavior within a short period of time. Reliable and efficient tools for predicting unsteady propeller forces as well as blade cavitation are needed in order to minimize design margins and to come close to an optimal solution. So far, tools based on the boundary element method (BEM) have successfully been applied for analyzing propeller designs – for both cavitating and non-cavitating flow conditions. The present work aims at enhancing the capabilities of BEM codes with respect to estimating the risk of cavitation erosion. For engineers exploring the design space towards highly efficient propellers, this can provide additional safeguarding against unfavorable cavitation patterns.

So far and to the authors' knowledge, numerous methods exist for estimating the erosion risk – all of which are based on analyzing the viscous cavitating flow around a given propeller design using viscous methods such as RANS or DES. An introductory overview has recently been given by Eskilsson and Bensow (2015). This procedure, however, entails an immense computational effort and is time-consuming – especially for unsteady flow configurations. Therefore, it is necessary to develop a faster alternative. Thus, an erosion risk index suitable for use within a potential theory-based panel code is formulated.

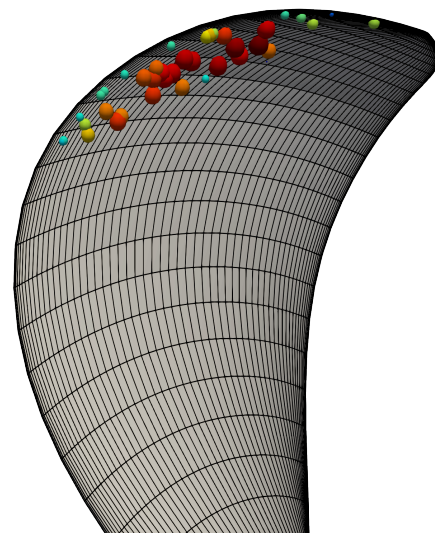


Figure 1: Idealized cavitation bubbles passing the blade surface of a marine propeller.

None of the so-called 'engineering' erosion models actually model the erosion process itself. Rather, by using specified criteria, the aggressiveness of the cavitating flow is evaluated, which is then related to the potential loss of material. The present method, however, may be particularly helpful to designers, especially in cases which compare a new blade design to an established design that has proven to be free of erosion.

The basic idea behind the present formulation of the erosion risk index – inspired by the so-called Discrete Bubble Method (e.g. Kato et al., 1996; Ochiai et al., 2009; Fukaya et al., 2010) – is to track spherical cavitation bubbles traveling along the blade surface and to study their behavior (see

*Corresponding author, e-mail: stephan.berger@man-es.com, phone: +45 33 85 10 65

Fig. 1). Abrupt shrinkage of the bubbles or even collapse on the blade surface are then interpreted as warning indicators for increased erosion risk. The method allows for investigating propellers in open water and propellers running in the inhomogeneous wake field of a ship. Furthermore, rudder erosion can also be addressed by the method.

In the following four sections, the erosion risk indicator is introduced and its computation is explained and presented. This paper starts with introducing the governing equations (Section 2). The implementation is sketched in Section 3. In Section 4, the results of a verification study, in which the influence of selected simulation parameters is tested, are shown. Finally, in Section 5, it is demonstrated how the erosion risk index can be used for erosion control in propeller design.

2 GOVERNING EQUATIONS

The Rayleigh-Plesset Equation models the behavior of a spherical cavity in free space. This equation is applied to approximate the behavior of cavitation bubbles traveling along the blade surface. In the present study, a generalized form of the equation, which takes into account liquid compressibility to a certain extent, is used (Franc and Michel, 2005b, pp. 78ff):

$$R\ddot{R}\left(1 - \frac{2\dot{R}}{c}\right) + \frac{3\dot{R}^2}{2}\left(1 - \frac{4\dot{R}}{3c}\right) = \frac{R}{\rho c} \frac{dP}{dt} + \frac{P - p}{\rho}. \quad (1)$$

Eq. (1) gives the time-dependent radius $R = R(t)$ of a cavitation bubble subjected to a surrounding pressure $p = p(\mathbf{x}_b, t)$. ρ and c are the (constant) density of liquid water and the speed of sound in water, respectively. Neglecting effects of surface tension and viscosity, the pressure P is given by:

$$P = p_v + p_g. \quad (2)$$

Here, p_v is the vapor pressure, and p_g is the partial pressure of noncondensable gases, which is modeled by assuming isothermal expansion and adiabatic compression (cf. Fukaya et al., 2010):

$$p_g = p_{g0} \left(\frac{R_0}{R}\right)^{3k} \quad \text{with } k = \begin{cases} 1 & \text{if } \dot{R} \geq 0 \\ \gamma & \text{if } \dot{R} < 0 \end{cases}, \quad (3)$$

with γ being the heat capacity ratio of the gaseous content of the bubble.

In the general case of a propeller flow, the bubbles are not at rest and their location \mathbf{x}_b changes. Their transport can be modeled by the following equation of motion (e.g. Abdel-Maksoud et al., 2010):

$$\frac{2}{3}\pi\rho R^3 \dot{\mathbf{u}}_b = \mathbf{F}_D + \mathbf{F}_p + \mathbf{F}_V, \quad (4)$$

where $\dot{\mathbf{u}}_b$ is the acceleration of the bubble; \mathbf{F}_D , \mathbf{F}_p and \mathbf{F}_V are the drag force, the pressure force and the volume force, respectively (see Section 3.3). Knowing $\dot{\mathbf{u}}_b$, the velocity of the bubble \mathbf{u}_b as well as its position \mathbf{x}_b can be found.

Eqs. (1) through (4) provide the framework for modeling the behavior of a ‘representative’ cavitation bubble traveling along the blade surface and being subjected to the blade

surface pressure field. It is important to note that modeling propeller cavitation – or even erosion – is not the intent of this study. Rather, it is assumed that by investigating the behavior of this ‘representative’ cavitation bubble, one can get an idea about the behavior of the real cavitation in terms of stability, growth and premature collapse, and hence possible erosion.

The acoustic pressure $p_a = p_a(t)$ radiated by the bubble in a distance d from the bubble center is derived by (Franc and Michel, 2005b, p. 83):

$$p_a = \frac{\rho}{4\pi d} \ddot{V}_{\text{bub}}(t - d/c), \quad (5)$$

with V_{bub} being the volume of the bubble. In the final stage of a collapse near to a solid wall, the radiated pressure can get very large. Eq. (5) is valid for the sound emission in the *far* field – a fact which is neglected in the following.

In order to formulate a suitable erosion risk index, it is necessary to relate the number of collapsing bubbles to the potential erosion damage. The hypothesis used here is that the erosion damage is proportional to the accumulated impact energy acting on the material (Okada et al., 1995; Franc and Michel, 2005a). The energy E of a single impact event is approximated by $E = \tau IA$ (Soyama et al., 2001), with I , A and τ being the acoustic intensity, the local surface area the impact acts on, and the impact duration, respectively. With $I = p_a^2 / (2\rho c)$ and assuming $\tau = \text{const.}$, one obtains

$$E \propto p_a^2 A \quad (6)$$

for the energy of a single impact. It is thus reasonable to formulate the following erosion risk index Π :

$$\Pi \propto \frac{1}{N_{\text{bub}}} \sum_{N_{\text{bub}}} \iint_{S_b} p_{a,\text{max}}^2 dS, \quad (7)$$

with S_b and N_{bub} being the blade surface and the number of bubbles released during the observation span, respectively; $p_{a,\text{max}}$ is the maximum of the acoustic pressure radiated by the respective bubble as given by Eq. (5). In other words, the higher the number of violent collapses on the blade surface, the higher is the risk of erosion for the propeller blade under consideration.

Preferably, the index developed here should be dimensionless. According to Franc (2007), the peak value of the acoustic pressure scales with $p_a \propto \rho \dot{R}^2$ during the collapse. For \dot{R} , it can be shown that $\dot{R} \propto \mathcal{V}$, with \mathcal{V} being a characteristic velocity of the flow configuration. In particular for propeller flow, $\mathcal{V} = nD$ is a good choice. Here, n is the number of revolutions and D is the propeller diameter. With $\iint_{S_b} dS \propto D^2$, a dimensionless form of the erosion risk index is obtained:

$$\Pi = \frac{1}{N_{\text{bub}} \rho^2 n^4 D^6} \sum_{N_{\text{bub}}} \iint_{S_b} p_{a,\text{max}}^2 dS. \quad (8)$$

The index defined by Eq. (8) quantifies the erosion risk in a global manner, i.e. a given flow configuration is evaluated by one single index. For a propeller designer, however, it is highly desirable to gain insight into the *distribution* of the erosion risk. This aspect is discussed in Section 3.5.

3 IMPLEMENTATION

To calculate the erosion risk index Π according to Eq. (8), a (possibly) large number of bubbles need to be observed as they travel over the blade surface, starting upstream the leading edge. Every single one of these bubbles has to be tracked and its evolution $R(t)$ has to be observed.

In the present approach, pressure and velocity on and around the propeller blades are given by the potential flow solution. For this purpose, the panel code ESPPRO, developed at Technical University of Denmark (DTU) and based on the boundary element method, is used (see Re-gener (2017) for details). The main difficulty with using ESPPRO for this application is that it uses a much coarser discretization with respect to time and space than what is required in order to numerically solve Eqs. (1), (4) and (5). This issue is addressed in detail in the following.

3.1 Coordinate System

Since only bubbles traveling along the blade surface are considered, it is convenient to introduce a problem-adapted coordinate system. For simplicity, only the suction side of the blade is considered here. It is regarded as a surface bounded by leading edge and trailing edge as well as hub and tip. Thus, a curvilinear coordinate system (ψ, ξ) is introduced with the local unit vectors \mathbf{t}_ψ and \mathbf{t}_ξ (see Figure 2).

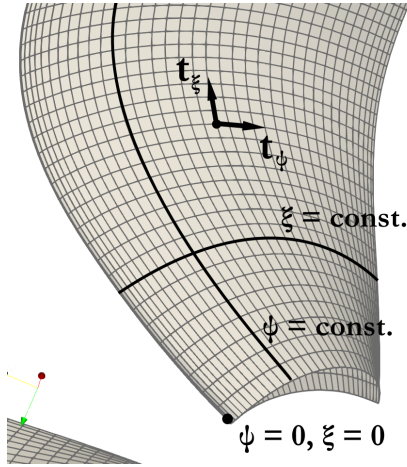


Figure 2: Adapted curvilinear coordinate system.

In order to define coordinate lines, use is made of the surface panels used by ESPPRO. The unit vector \mathbf{t}_ψ is locally aligned with the panel edges pointing in the main flow direction from leading edge to trailing edge; \mathbf{t}_ξ points from hub to tip and is locally aligned with the corresponding panel edges. The origin $\psi = 0$, $\xi = 0$ is defined to be located at the leading edge at the propeller hub.

3.2 Potential Flow Solution

Evaluating the erosion risk is performed independent of finding the potential flow solution; however, the potential flow solution is used to evaluate the erosion risk. The results with respect to erosion risk do not have any influence on the potential flow solution. Therefore, in the remainder

of the text, the potential flow solution in terms of pressure p and velocity \mathbf{v} is considered as known:

$$p(\psi, \xi, t) \text{ and } \mathbf{v}(\psi, \xi, t). \quad (9)$$

Here, ψ and ξ denote the coordinates in the local ‘panel-aligned’ coordinate system (see previous subsection). The time variable is t ; p is the pressure on the blade surface, and $\mathbf{v} = (v_\psi, v_\xi)$ is the velocity on the surface in the direction of \mathbf{t}_ψ and \mathbf{t}_ξ , respectively.

3.3 Bubble Transport and Bubble Dynamics

Bubbles are transported along the blade surface, primarily following the direction of the main flow. The forces acting on the bubble are – see Abdel-Maksoud et al. (2010) for details – the drag force \mathbf{F}_D with

$$\mathbf{F}_D = -C_D \frac{\rho}{2} \pi R^2 \|\mathbf{u}_b - \mathbf{v}\| (\mathbf{u}_b - \mathbf{v}), \quad (10)$$

where C_D is the drag coefficient, the force due to the pressure gradient \mathbf{F}_p with

$$\mathbf{F}_p = -2\pi R^3 \nabla p, \quad (11)$$

where $\nabla = \left(\frac{\partial}{\partial \psi}, \frac{\partial}{\partial \xi} \right)$, and the volume force \mathbf{F}_V , which is given by:

$$\mathbf{F}_V = -2\pi \rho R^2 \dot{R} (\mathbf{u}_b - \mathbf{v}). \quad (12)$$

Eq. (4) can then be solved using a Runge-Kutta scheme with the initial velocity $\mathbf{u}_{b0} = \mathbf{v}$ at the initial position \mathbf{x}_{b0} .

Also by means of a Runge-Kutta scheme, Eq. (1) can be solved for each bubble, taking into account $p = p(\mathbf{x}_b, t)$ in order to find R , \dot{R} and \ddot{R} . The bubbles are assumed to be very close, with a constant distance δ , to the surface. However, in order to further simplify the procedure, the surface pressure and velocity at \mathbf{x}_b are used, and any normal distance to the surface is neglected when evaluating pressure and velocity acting on the bubbles.

3.4 Discretization and Interpolation

In order to numerically solve the problem, discretization in time and space are required. The potential flow solution found by ESPPRO is known only at discrete instants of time t_k with $\Delta t = t_k - t_{k-1}$ as well as discrete points on the surface, i.e. collocation points, $\mathbf{x}_i = (\psi_i, \xi_i)$; hence:

$$p(\psi_i, \xi_i, t_k) \text{ and } \mathbf{v}(\psi_i, \xi_i, t_k). \quad (13)$$

However, in order to resolve bubble dynamics and trajectory given by Eqs. (1) and (4) as well as to evaluate Eq. (8), a second, finer time discretization level \tilde{t}_i is introduced, with

$$\frac{\Delta t}{\Delta \tilde{t}} = \frac{t_k - t_{k-1}}{\tilde{t}_i - \tilde{t}_{i-1}} = 10^4 \dots 10^6, \quad (14)$$

depending on the particular case. Especially during the shrinking process, a small time step size is required for properly capturing the high gradients of $R(t)$, which can be computationally expensive. An adaptive time step size is thus introduced for the Runge-Kutta scheme. From one time step to the next time step the bubble may shrink by an

increment $\Delta R > 0$. The time step size $\Delta \tilde{t} = \Delta \tilde{t}_l$ is adapted by limiting this increment:

$$\frac{\Delta R_{\max}}{|\dot{R}(\tilde{t}_{l-1})| + \kappa} \rightarrow \Delta \tilde{t}_l, \quad (15)$$

for every bubble j during the shrinkage process, with κ being a reasonable small number. The scheme requires specifying an interval $[\Delta \tilde{t}_{\min}, \Delta \tilde{t}_{\max}]$ for limiting $\Delta \tilde{t}_l$ to a lower and upper boundary.

As bubbles are traveling over the blade surface independent of the panel grid, interpolation with respect to location is needed. This is shown in Fig. 3.

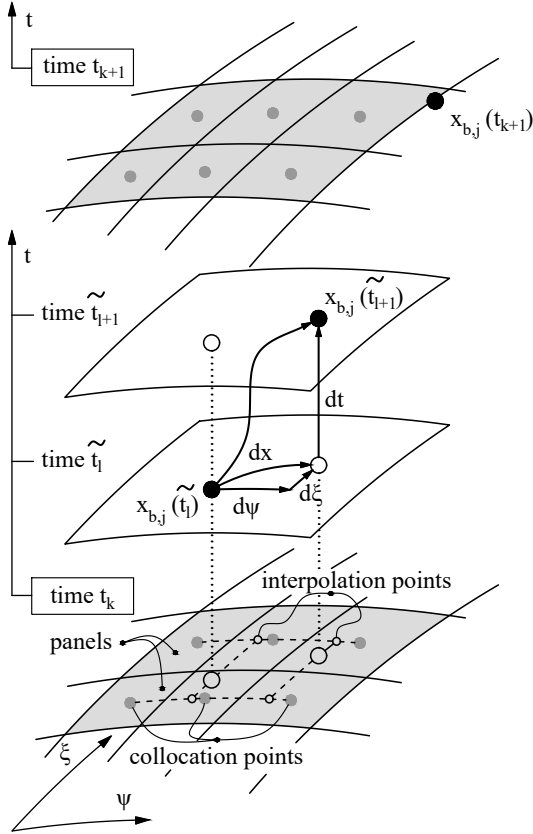


Figure 3: Interpolation scheme.

In order to find pressure and velocity acting on the j -th bubble at $\mathbf{x}_{b,j}$, it is necessary to map these quantities from $\mathbf{x}_i = (\psi_i, \xi_i)$ to $\mathbf{x}_{b,j} = (\psi_{b,j}, \xi_{b,j})$. First, the interpolation partners need to be found, i.e. the nearest four collocation points for which $\psi_i \leq \psi_{b,j} \leq \psi_{i+1}$ and $\xi_i \leq \xi_{b,j} \leq \xi_{i+1}$ are fulfilled. Making use of auxiliary interpolation points, the flow quantities are first interpolated in the direction of ψ and then in the direction of ξ . The position $\mathbf{x}_{b,j}$ of the bubble can be updated every time step \tilde{t}_l . In order to increase computational efficiency, however, it is beneficial to skip a suitable number of inner time steps – especially when $\Delta \tilde{t}_l$ becomes small.

The unsteady flow field is updated every time step t_k . This is assumed to be accurate enough as long as the time discretization on the t_k -level (capturing the propeller flow) is fine enough.

3.5 Evaluation of Acoustic Pressure

As mentioned in Section 2, the radiated acoustic pressure of a bubble has to be evaluated. It is assumed that a significant pressure impact only occurs during the collapse of a bubble and thus only shrinking/collapsing bubbles have to be taken into account. The assumption of a spherical bubble collapse close to the propeller surface is clearly an oversimplification. However, since it is far beyond the intention of this study to model the actual erosion process, it is believed that a rough estimate of the maximum collapse pressure is sufficient for the present purpose.

For a bubble being released at the leading edge and traveling over the blade surface, there are two scenarios considered which might set in after a growing phase of the bubble:

- (1) The bubble grows and reaches the trailing edge before shrinking/collapsing significantly, i.e. $\dot{R} > 0$ all the time or $R > \beta R_{\max}$ for $\dot{R} < 0$ with reasonable values for β , say, $\beta = 1/3$, for example.
- (2) A significant shrinkage most likely followed by a collapse sets in. This is detected when the following criteria are fulfilled during the bubble's passage on the blade: $\dot{R} < 0$ and $R < \beta R_{\max}$.

Only bubbles fulfilling the second condition are considered; others are excluded from subsequent procedures. Since cavity rebounds are known for being much less violent compared to the first collapse (cf. e.g. Brennen, 2002; Ross, 1976; Zhang et al., 1989), the simulation of a bubble is stopped after the first collapse.

With progressing collapse, it is assumed that any displacement of the bubble is negligible. Updating the bubble position and the surrounding pressure as described in Section 3.4 is thus stopped as soon as the bubble radius falls below $R < \beta R_{\max}$.

With $V_{\text{bub}} = 4/3\pi R^3$ used in Eq. (5), the acoustic pressure radiated by a bubble at a distance d to the bubble center gets:

$$p_a = \frac{\rho}{d} (R^2 \ddot{R} + 2R\dot{R}^2). \quad (16)$$

According to the theory of spherical bubble collapse, the maximum radiated pressure $p_{a,\max}$ is reached when $R = R_{\min}$ (Tomita and Akira, 1977). In this case, $\dot{R} = 0$ and \ddot{R} reaches large positive values. During collapse, the gradients of $R(t)$ can get very high, while R reaches extremely small values.

In order to avoid overly fine time step sizes, the simulation stops when the bubble reaches a certain threshold radius $R \leq R_{\text{lim}}$. Certainly, the radiated pressure during such a ‘truncated’ collapse will be deviant from the radiated pressure peak which is emitted during the complete collapse. However, it is possible to estimate the collapse pressure $p_{a,\max}$ based on \dot{R}_{\max} shortly before the collapse, i.e. when $\ddot{R} = 0$. It can be shown that for a bubble containing an amount of noncondensable gas, the maximum radiated pressure during collapse depends mainly on the ratio between maximum and minimum bubble radius, R_{\max} and

R_{\min} , as well as on the surrounding pressure during collapse (Ross, 1976, p. 218):

$$p_{a,\max} \approx \frac{p^* R_{\max}}{3d} \left(\frac{R_{\max}}{R_{\min}} \right)^2, \quad (17)$$

where $p^* = |p(\mathbf{x}_{bc,j}) - p_v|$ and d is the distance to the bubble center. Based on the same assumptions, it is possible to relate the maximum interface velocity \dot{R}_{\max} on R_{\max}/R_{\min} (Ross, 1976, pp. 209ff):

$$\dot{R}_{\max}^2 = \frac{1}{12} \frac{p^*}{\rho} \left(\frac{R_{\max}}{R_{\min}} \right)^3. \quad (18)$$

Combining Eqs. (17) and (19) leads to:

$$p_{a,\max} \approx M \frac{R_{\max}}{d} [\rho^2 p^* \dot{R}_{\max}^4]^{1/3}, \quad (19)$$

with $M = 1.747$. This formula is derived based on the assumption of incompressible flow; however, it will be shown in Section 4.1 that reasonable results can be obtained for compressible flow, too.

3.6 Evaluation of the Erosion Risk Index

In this subsection, the procedure for evaluating the erosion risk index according to Eq. (8) is explained. In the following, it is assumed that the j -th bubble experiences a significant collapse.

In this case, the maximum acoustic pressure $p_{a,\max}^{[\delta,j]}$ radiated at a distance $d = \delta$ is evaluated either by Eq. (16) for $\dot{R}_j = 0$ and large positive values of \ddot{R}_j , or, it is approximated by Eq. (19) without the necessity of resolving the entire collapse. Here, a reference distance is used, which is chosen to be the orthogonal distance δ between bubble and propeller surface (see Section 3.3).

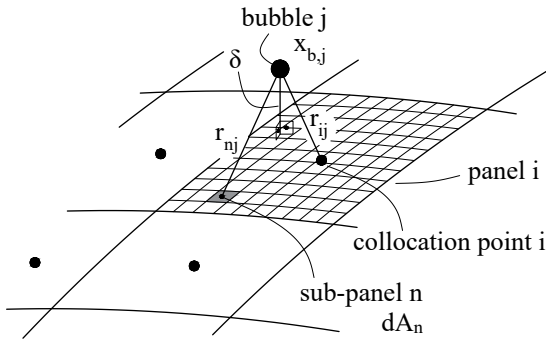


Figure 4: Evaluation of the integral in Eq. (20).

It is possible to introduce a threshold to Eq. (8) in order to take into account that low pressure pulses will not contribute to erosion (e.g. Soyama et al., 2001). With ε being a suitable threshold value, two scenarios are considered:

- (1) If $p_{a,\max}^{[\delta,j]} < \varepsilon$, the bubble is disregarded since there is no possibility that the threshold ε can be exceeded at any location on the blade. With this procedure, non-relevant bubbles are directly filtered out, helping to reduce the computational effort.

- (2) If $p_{a,\max}^{[\delta,j]} \geq \varepsilon$, the impact of the bubble collapse is considered by the procedure, which is explained in the following.

For every bubble j fulfilling the second condition, the impact on the i -th panel π_{ij} is calculated:

$$\pi_{ij} = C B_{ij} \iint_{A_i} \left(p_{a,\max}^{[ij]} \right)^2 dA. \quad (20)$$

Again, the threshold value ε is applied by introducing the factor B_{ij} in Eq. (20):

$$B_{ij} = \begin{cases} 1 & \text{if } p_{a,\max}^{[\delta,j]} \frac{\delta}{r_{ij}} > \varepsilon \text{ during collapse of bubble } j, \\ 0 & \text{otherwise} \end{cases} \quad (21)$$

with $r_{ij} = \|\mathbf{x}_i - \mathbf{x}_{b,j}\|$ being the distance between the j -th bubble at $\mathbf{x}_{b,j}$, when $p_{a,\max}^{[\delta,j]}$ is radiated, and the panel center \mathbf{x}_i . The factor

$$C = \frac{1}{\rho^2 n^4 D^6} \quad (22)$$

in Eq. (20) is applied to obtain a dimensionless quantity (see Section 2 for an explanation).

In order to evaluate the integral in Eq. (20), the i -th panel is divided in N_{sub} sub-panels. The integral can then be approximated by:

$$\iint_{A_i} \left(p_{a,\max}^{[ij]} \right)^2 dA_i \approx \left(p_{a,\max}^{[\delta,j]} \right)^2 \delta^2 \sum_{n=1}^{N_{\text{sub}}} \frac{1}{r_{nj}^2} dA_n, \quad (23)$$

where $r_{nj} = \|\mathbf{x}_n - \mathbf{x}_{b,j}\|$ and \mathbf{x}_n is the center of the n -th sub-panel of the i -th panel. Note that, by definition, $r_{nj}, r_{ij} \geq \delta$, i.e. r_{nj}^{-2} cannot become singular. The scheme is illustrated in Fig. 4.

In order to depict the *distribution* of erosion risk on the blade surface and to highlight locations of increased erosion risk, it is suitable to look at the accumulated panelwise erosion risk index. For the i -th panel, one obtains:

$$\pi_i = \frac{1}{N_{\text{bub}}} \sum_{j=1}^{N_{\text{bub}}} \pi_{ij}. \quad (24)$$

The global erosion risk index Π , which has been introduced in Section 2, is yielded simply by summation over all N_{pan} panels:

$$\Pi = \sum_{i=1}^{N_{\text{pan}}} \pi_i. \quad (25)$$

3.7 Initialization of the Bubbles

In general, water is populated by bubbles of various sizes R_0 and concentration $c_{\text{vol}} = \text{bubbles/unit volume}$. It will be demonstrated in Section 4.1 that the initial conditions for a bubble in terms of R_0 and p_{g0} have an impact on the results. At the same time, however, there is no rationale to choose specific values for these initial conditions. Hence, inspired by nature, the bubbles are randomly initialized.

At every time step t_k , a new group of bubbles is released and initialized at the leading edge of the propeller blade. With the bubble concentration c_{vol} as input parameter, it is possible to estimate the number of bubbles n_{bub} to be released per time step t_k in a simple manner by

$$n_{\text{bub}} = c_{\text{vol}}^{2/3} \Delta A_s, \quad (26)$$

where

$$\Delta A_s \approx \frac{\Delta t}{2} \left(\frac{D}{2} - r_{\text{min}} \right) \left(V_e \left(\frac{D}{2} \right) + V_e(r_{\text{min}}) \right) \quad (27)$$

is the sectional area the propeller blade sweeps at one time step. Here, $V_e = V_e(r)$ is the effective flow velocity faced by the blade at radius r . It is possible to limit the release zone by an inner radius r_{min} , which excludes the hub region from the simulation.

For the initial bubble position, a uniform distribution is considered. Somewhat deviating from nature, the initial bubble size $R_{0,j}$ is assumed to be uniformly distributed over an interval $[R_{0,\text{min}}, R_{0,\text{max}}]$, where suitable values for the interval boundaries have to be selected by the user.

The rationale behind this assumption is that bubbles impinging the propeller surface can be both bubbles present in the water and the remainders of disintegrating cavitation formations on the propeller blades. This combination comprises a wide range of initial bubble sizes. The initial partial pressure of noncondensable gases p_{g0} is considered as a model parameter that needs to be defined by the user. This aspect is discussed in Section 4.1.

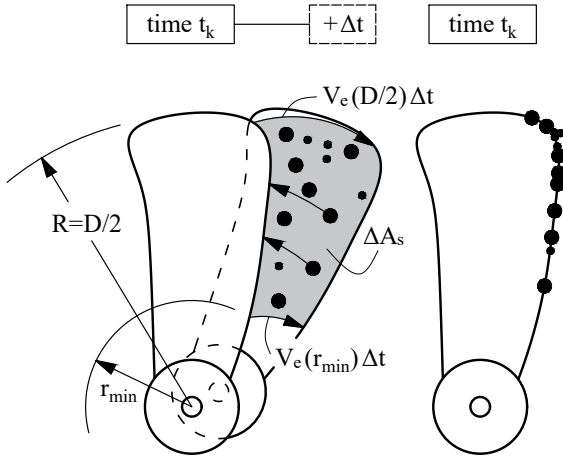


Figure 5: Initialization of bubble radius and position.

As the initialization is only carried out once per time step t_k , the actual angular position of the bubbles during initialization does not play a role. Rather, all n_{bub} bubbles located at their initial positions upstream the leading edge are ‘shifted’ towards their initial position $\mathbf{x}_{b0,j} = (0, \xi_{b0,j})$ at the leading edge while maintaining their individual radial position (see Fig. 5). This obviously leads to more bubbles in the tip region compared to regions which are closer to the propeller hub.

4 VERIFICATION

In this section, the simulation method is verified and some particularities of the model important for interpreting the results regarding erosion risk are explained. For this purpose, Propeller P1.1, a propeller variant exhibiting a high likelihood of bubble collapse, has been selected. This propeller has never been built and is used mainly for the purpose of demonstrating the capabilities of the new simulation method. The main dimensions and operation conditions can be found in Table 1. All simulations are carried out for full-scale conditions.

4.1 Behavior of a Single Bubble

The verification study starts with focusing on a single bubble. In the present scenario, the bubble grows while passing a zone of low pressure in the blade tip region and collapses in a high-pressure zone further downstream. An exemplary result is shown in Fig. 6. For the case considered here, the difference obtained for compressible flow and incompressible flow ($c \rightarrow \infty$) is only visible by magnification. For the case of incompressible flow, it can be seen that the bubble shrinks to a smaller size and that \dot{R} reaches higher values. Furthermore, in the second magnification, it can be seen how \dot{R} approaches zero when R reaches the minimum.

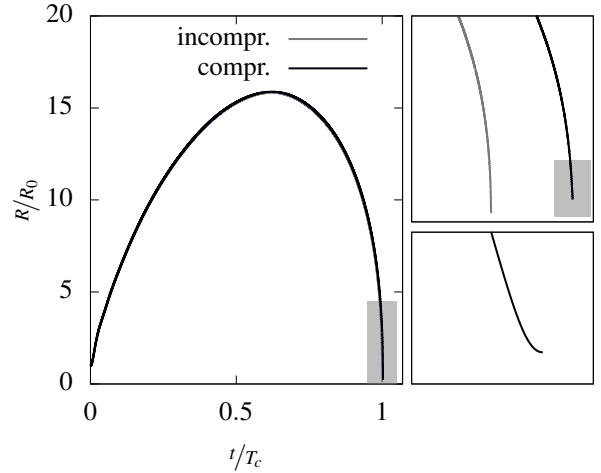


Figure 6: Behavior of a single bubble entering a high-pressure zone after passing a zone of low pressure. Two magnifications are shown.

The simulation has been repeated for a number of single bubbles with different initial radius R_0 , ranging from $5 \cdot 10^{-4}$ m to 10^{-2} m, and different partial pressures of noncondensable gases p_{g0} (here: 10^3 Pa, 10^4 Pa and $5 \cdot 10^4$ Pa) for otherwise identical conditions. All bubbles grow to a maximum radius, at which the partial pressure of noncondensable gases becomes minimum. The value of $p_{g,\text{min}}$ depends on the pairing of R_0 and p_{g0} (see Eq. (3)). It is a well known fact that noncondensable gases have the effect of a ‘cushion’ and can significantly dampen the collapse. This is also confirmed by the results presented in Fig. 7. Here, the effect of gas content on the maximum of acoustic pressure is demonstrated: the lower the content of noncondensable gases, the higher the acoustic pressure and

the larger the difference between compressible and incompressible solution.

The rough estimate of $p_{a,\max}$ by Eq. (19) leads to a good agreement for sufficiently high gas contents. For lower gas contents, the bubble radius gets so small that the lower limit $R \leq R_{\text{lim}}$ (see Section 3.5) is hit and the simulation is aborted before the bubble reaches the minimum radius. This is denoted by the void circles in Fig. 7. In these cases, using the estimation formula might lead to more realistic results than using Eq. (16).

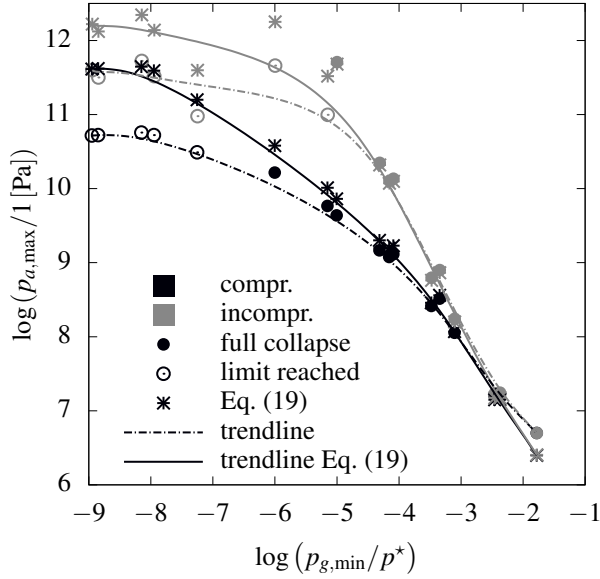


Figure 7: Influence of compressibility and noncondensable gases on acoustic pressure radiated by a single bubble; $p^* = p - p_v$ as in Eq. (17).

This simulation campaign involving a single bubble illustrates a major issue in the present formulation of the erosion risk index. By simply changing the initial values for R_0 and p_{g0} , the radiated pressure $p_{a,\max}$ can change by five orders of magnitude for otherwise completely identical conditions. It is thus necessary to provide information on bubble size and gas content when comparing the erosion risk indices of two different design variants. Furthermore, it is advised to only choose pairings of R_0 and p_{g0} leading to sufficiently large gas content in order to avoid extreme collapses, which might tamper with the significance of the erosion risk index.

4.2 Influence of Number of Bubbles

In this simulation campaign, the influence of bubble concentration on the results is investigated. For this purpose, the bubble concentration in terms of n_{bub} has been varied (here: 1, 5, 15, 25 and 50). Furthermore, five choices of initial bubble radius R_0 have been tested: $5 \cdot 10^{-4}$ m, 10^{-3} m, $5 \cdot 10^{-3}$ m and 10^{-2} m and random initialization using the interval $[5 \cdot 10^{-4} \text{ m}, 10^{-2} \text{ m}]$. The partial pressure of noncondensable gases has been chosen to be $p_{g0} = 3 \cdot 10^4$ Pa for all cases, and the initial position of the bubble is chosen randomly as described in Section 3.7.

The results of the study are compiled in Fig. 8. As a measure for the convergence, the quantity $N_{\text{bub}}^{-1} \sum p_{a,\max}^2$ is used. The solution does not change significantly for $n_{\text{bub}} \geq 25$. In accordance with the findings of the previous subsection, small bubbles cause large peaks of acoustic pressure during collapse. Again, it is advised to avoid too small initial values for R_0 , which may result in overly high pressure peaks.

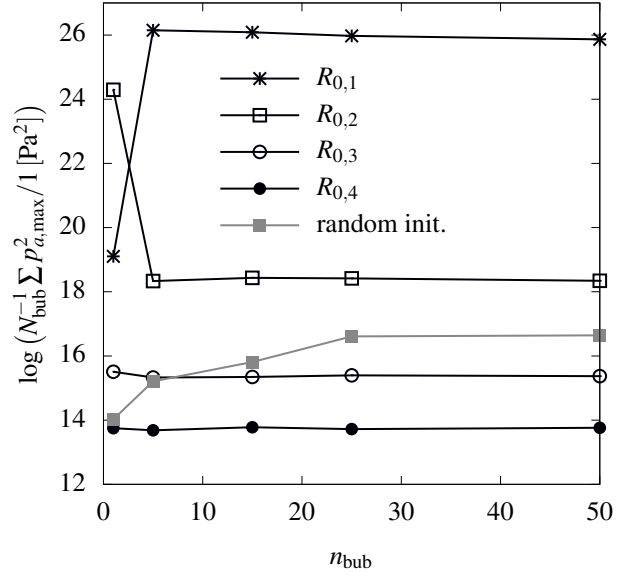


Figure 8: Influence of bubble concentration in terms of n_{bub} for different choices of R_0 ; $R_{0,1} = 5 \cdot 10^{-4}$ m, $R_{0,2} = 10^{-3}$ m, $R_{0,3} = 5 \cdot 10^{-3}$ m and $R_{0,4} = 10^{-2}$ m.

5 CASE STUDIES

In this section, the method's ability for erosion risk control is demonstrated. For this purpose, propeller design variants from two different projects, P1 and P2, are evaluated with respect to erosion risk.

5.1 Validation with DES Erosion Risk Analysis

In order to validate the developed method, results are compared to the results obtained by a DES analysis of the erosion risk using the simulation software StarCCM+. Here, cavitation is modeled by a volume-of-fluid (VOF) method, a generic transport equation for the vapor volume fraction α and an interphase mass transfer model based on the asymptotic Rayleigh-Plesset Equation. This method has been validated against cavitation tunnel test results for different types of propeller cavitation. For details, also on the numerical setup, see Shin and Andersen (2015) as well as Shin et al. (2015).

In the present study, an erosion risk index based on $\alpha \cdot \max\{(p - p_v), 0\}$ as proposed by Hasuike et al. (2009) is used for comparison. It has been implemented making use of StarCCM+ User Coding. Physically, the formulation can be related to the potential energy of a local cavitation structure, which is considered as a measure for the aggressiveness of the local flow.

It should be noted that cavitation erosion risk is more often assessed by considering the potential power of a cavity collapse instead of the potential energy (e.g. Hasuike et al., 2009; Li and van Terwisga, 2012). However, numerical tests carried out for a wide range of commercial propeller designs show a better agreement with experimental results from paint tests for the formulation based on the potential energy.

Obviously, a direct comparison of the results obtained by the DES analysis and the method developed here is difficult since both methods are based on very different approaches. Currently, one is thus restricted to a purely visual manner of comparison. For this reason, no color scale is given for the results of the DES analysis in the following.

5.2 Numerical Set-Up

In Fig. 9, the panelization of the investigated propeller variants is depicted. For all cases, the same grid topology has been used: 30 panels in the spanwise direction and $2 \cdot 58$ panels on suction and pressure side in the chordwise direction. The grid density is chosen to be high at the leading edge and at the trailing edge in order to properly resolve the large gradients of pressure in these regions. The time step size Δt for simulating the propeller flow has been adjusted such that the propellers rotate 1° per time step.

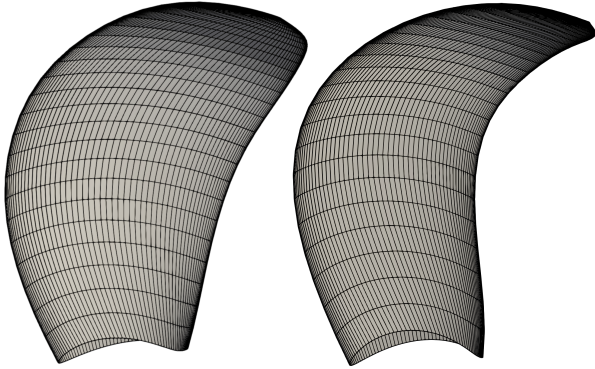


Figure 9: Panelization of the investigated propellers. One variant of each propeller is shown. Left: P1; right: P2.

All simulations are carried out for the full-scale propeller, and the influence of hydrostatic pressure is taken into account. For all simulations, c_{vol} has been chosen such that $n_{bub} = 15$ bubbles are released at the leading edge per time step Δt .

Initial bubble sizes R_0 are uniformly distributed over the interval $[2 \cdot 10^{-3} \text{ m}, 10^{-2} \text{ m}]$, and $p_{g0} = 5 \cdot 10^4 \text{ Pa}$ has been used in all cases. Collapses with acoustic pressures $p_{a,max} < \varepsilon$ with $\varepsilon = 5 \cdot 10^6 \text{ Pa}$ are not considered as contributors to the erosion risk (see Section 3.6).

5.3 Results for Kappel Propeller P1

The first propeller design, Propeller P1, is a Kappel propeller. This propeller type exhibits a ‘bent’ tip, which is beneficial for the propulsive efficiency (Andersen et al., 2005). However, cavitation becomes more pronounced at the propeller tip and erosion control is important for these

highly efficient propellers. The main dimensions of the propeller and its variants are listed in Tab. 1. The variants differ only in the local design of the blade tip.

Table 1: Main dimensions and operation conditions for Propeller P1 and its variants.

Characteristics			Value
<i>Propeller P1</i>			
Variants	P1.1, P1.2, P1.3		
Type, sense of rot.	1 × FPP Kappel-type, clockwise		
Propeller diameter	$D = 2R$	[m]	9.000
Number of blades	n_z	[-]	5
Hub ratio	d_h/D	[-]	0.180
Area ratio	$A_e/(\frac{\pi}{4}D^2)$	[-]	0.652
Pitch ratio	$P_{0.7}/D$	[-]	1.070
<i>Operation conditions</i>			
Rate of rev.	n	$[s^{-1}]$	1.379
Ship speed	V_s	$[m/s]$	12.410
Wake fraction	w	[-]	0.188
Advance coefficient	J	[-]	0.812
Cavitation number	σ_n	[-]	2.320

In order to analyze the propeller design variants with respect to erosion risk, refer to the graphical representation shown in Figs. 14, 15 and 16 at the end of this paper.

Both methods, the newly developed method (sub-figures b) and the erosion risk prediction based on DES (sub-figures c), show the same trends for all three variants. The initial variant P1.1 exhibits an increased erosion risk at the blade tip. For variant P1.2, the erosion risk could be reduced, and the improved design P1.3 has the lowest erosion risk. In general, the DES analysis predicts the spots of increased erosion risk to be located somewhat more upstream.

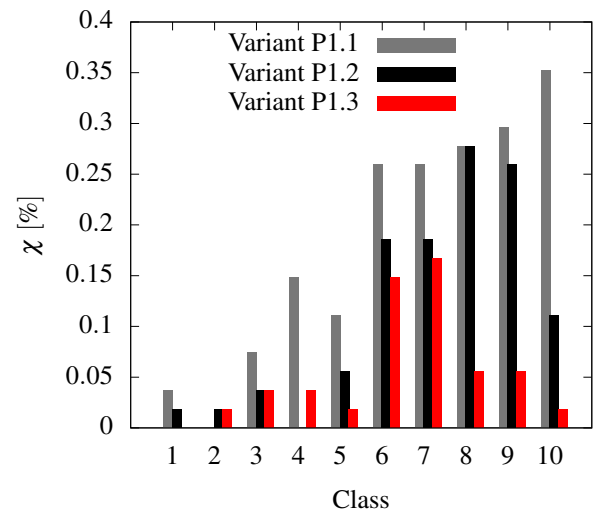


Figure 10: Statistics of bubble collapses for P1.1, P1.2 and P1.3 with $\chi = n_{class}/N_{bub}$. See text for explanation on the classification.

Furthermore, all collapses observed during simulation of P1.1, P1.2 and P1.3 with $p_{a,max} > \varepsilon$ have been sorted starting from the lowest to the highest value. This list has then

been divided into classes, such that class 1 contains the lowest 10% in terms of collapse intensity and class 10 resembles the last 10% with the highest collapse pressure observed during the simulation campaign.

It can be seen in Figs. 14a, 15a, 16a as well as in the histogram in Fig. 10 that the number of intensive collapse events decreased when comparing the initial variant P1.1 and the improved design variant P1.3.

Table 2: Global erosion risk index Π for the variants P1.1, P1.2 and P1.3 of Propeller P1.

Propeller P1			
Variant	Π	$\Pi/\Pi_{P1.1}$	Risk reduction
P1.1	$2.55 \cdot 10^{-1}$	100.0%	
P1.2	$3.49 \cdot 10^{-2}$	13.7%	-86.3%
P1.3	$9.92 \cdot 10^{-3}$	3.9%	-96.1%

The global erosion risk index Π is listed in Tab. 2 for the three design variants. It can be seen that the risk for erosion could be decreased by 96.1%. However, care must be exercised when interpreting these numbers. In every case, the panelwise erosion risk index π_i and the statistics on bubble collapses should be studied diligently before drawing any conclusions.

5.4 Influence of Wake Field and Operation Conditions

In order to study the influence of operation conditions and the ship's wake field, a number of additional simulations have been carried out for Propeller P1.1. These simulations involve decreasing and increasing the advance coefficient by 3% as well as replacing the ship's wake field by homogeneous inflow.

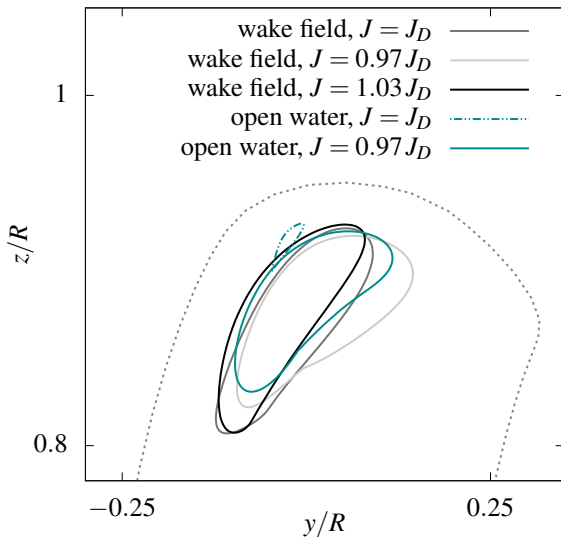


Figure 11: Influence of operation conditions and the ship's wake field on the extent of the region with increased number of bubble collapses. Results for Propeller P1.1; curve smoothing has been applied.

In Fig. 11, it can be seen how the region with increased number of bubble collapses is shifted when changing the

advance coefficient. When decreasing the advance coefficient (i.e. *increasing* the blade load), the region is shifted downstream. This is not surprising since zones of low pressure on the blade extend further downstream when the blade load is increased. For the same reason, increasing the advance coefficient causes the opposite effect: The region of increased number of bubble collapses is slightly shifted to the leading edge.

When homogeneous inflow is considered instead of the ship's wake field, almost no bubble collapses can be detected on the blade in the present case (see dashed turquoise contour line in Fig. 11). In order to be able to observe some collapses in homogeneous inflow as well, the propeller load must be increased.

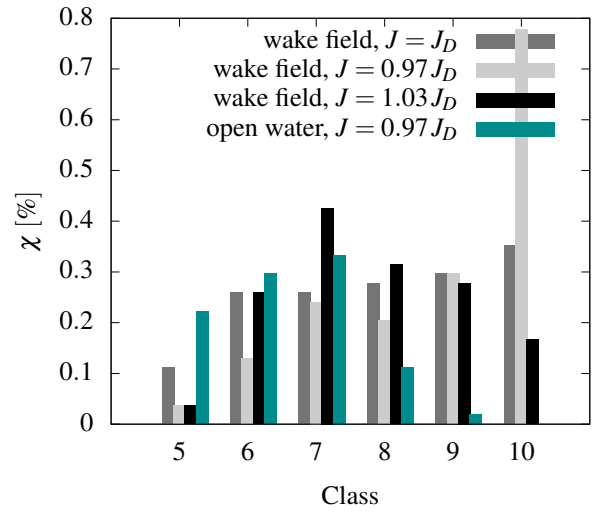


Figure 12: Statistics of bubble collapses for P1.1 with $\chi = n_{\text{class}}/N_{\text{bub}}$; influence of operation conditions and the ship's wake field.

The classification shown in Fig. 12 is based on the same class intervals as used in Fig. 10. Increasing the blade load leads to more class-10 collapses on the blade. Contrarily, decreasing the blade load decreases the intensity of collapses. In homogeneous inflow, highly intensive collapses cannot be observed any more in the present case. This investigation demonstrates how important it is to consider the ship's wake field when making a reliable prognosis of the erosion risk.

5.5 Results for Kappel Propeller P2

The second example, Propeller P2, originates from a challenging project. Tab. 3 compiles the main dimensions of this propeller. The area ratio is very small – it has only three blades and a reduced chord length. This results in a high propulsive efficiency; however, it also requires very careful control of cavitation and erosion. Here, this is complicated by the unfavorable wake field the propeller works in ($w = 0.269$).

The two variants, P2.1 and P2.2, differ primarily in the local design of the propeller tip. The improvement between the two variants is demonstrated in Figs. 17 and 18. Variant

P2.1 has a relatively high ratio between thickness and chord length at the tip, which causes an unfavorable pressure distribution. In Fig. 17a, a dense accumulation of collapses at the blade ‘tail’ can be noted. This accumulation results in an increased erosion risk at this region. As a conclusion, the blade thickness has been reduced for the improved design, which yields P2.2.

Table 3: Main dimensions and operation conditions for Propeller P2 and its variants.

Characteristics			Value
<i>Propeller P2</i>			
Variants	P2.1, P2.2		
Type, sense of rot.	1 × FPP Kappel-type, clockwise		
Propeller diameter	$D = 2R$	[m]	7.200
Number of blades	n_z	[-]	3
Hub ratio	d_h/D	[-]	0.174
Area ratio	$A_e/(\frac{\pi}{4}D^2)$	[-]	0.349
Pitch ratio	$P_{0.7}/D$	[-]	0.963
<i>Operation conditions</i>			
Rate of rev.	n	$[s^{-1}]$	1.533
Ship speed	V_s	$[m/s]$	9.554
Wake fraction	w	[-]	0.269
Advance coefficient	J	[-]	0.633
Cavitation number	σ_n	[-]	2.530

For the classification of collapses, the same procedure as described in Section 5.3 has been applied using all collapses observed during the simulation of P2.1 and P2.2 with $p_{a,max} > \varepsilon$ as base. According to the histogram in Fig. 13, the number of collapses has shrunk tremendously for P2.2; however, there is an increase of intensive collapse events. Since these collapses do not occur concentrated at one spot, their effect on the erosion risk is not critical.

The results discussed so far and the results obtained by DES analysis (see Figs. 17c and 18c) are in fairly good agreement.

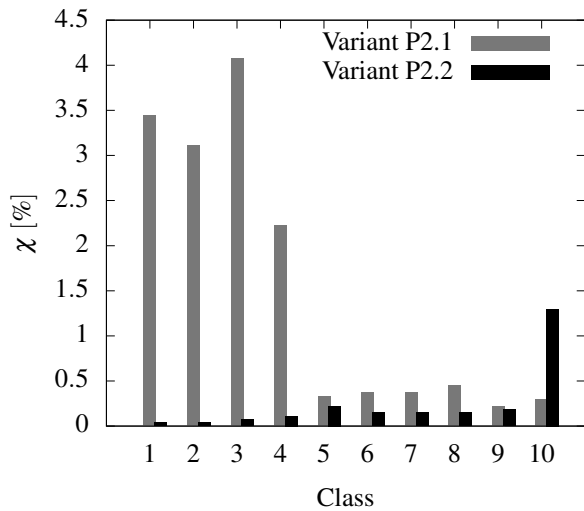


Figure 13: Statistics of bubble collapses for P2.1 and P2.2 with $\chi = n_{class}/N_{bub}$. See Section 5.2 for explanation on the classification.

The global erosion risk Π could be reduced by 96.9% (see Tab. 4) by decreasing the ratio between thickness and chord length at the tip. It should be noted that the requirements for the structural integrity impose limitations on reducing blade thickness.

Table 4: Global erosion risk index Π for the variants P2.1 and P2.2 of Propeller P2.

<i>Propeller P2</i>			
Variant	Π	$\Pi/\Pi_{P2.1}$	Risk reduction
P2.1	$4.32 \cdot 10^{-4}$	100.0%	
P2.2	$1.35 \cdot 10^{-5}$	3.1%	-96.9%

CONCLUSIONS

A method for evaluating the erosion risk of marine propellers has been presented. The method is based on studying the behavior of single bubbles as they pass the propeller surface. Growth and shrinkage of these bubbles are analyzed and violent collapses are assumed to be warning indicators for potential erosion and unfavorable pressure distributions on the blade. The propeller flow is simulated by means of DTU’s panel code ESPPRO, which makes the method particularly fast and efficient compared to alternative and more sophisticated concepts based on viscous flow simulations. Whereas DES erosion analysis, for example, requires a couple of days on a cluster, the newly developed method runs on ordinary desktop computers and delivers results within half an hour.

The agreement between results obtained by the newly developed method and well-established erosion indicators based on DES analysis is surprisingly good – especially when having in mind the simplicity of the present approach. Furthermore, the simulations carried out highlight the great importance of properly representing the ship’s wake field when analyzing the erosion risk.

Different ways of visualization have been introduced, and it has been advised to use all of them in a combined manner in order to reliably gain insight into the erosion risk of a propeller design variant.

NOMENCLATURE

General variables and constants

$\mathbf{x} = (\psi, \xi)$	Space variable in curvilinear coordinate system on propeller surface
ψ, ξ	Spanwise coordinate, chordwise coordinate
t	Time variable
ρ	Density of water
c	Speed of sound in water
p_v	Vapor pressure of water

Outer flow problem

$\mathbf{v}(\psi, \xi, t)$	Total velocity in curvilinear coordinates (ψ, ξ)
$p(\psi, \xi, t)$	Pressure on the blade

<i>Bubble dynamics</i>	
R, \dot{R}, \ddot{R}	Bubble radius, first and second derivative of R with respect to time t
p_g	Partial pressure of noncondensable gases
P	Pressure in the bubble
k	Polytropic exponent
γ	Heat capacity ratio
p_a	Acoustic pressure radiated by a bubble
V_{bub}	Volume of a cavitation bubble
d	Distance to bubble center
\mathbf{x}_b	Bubble position
\mathbf{u}_b	Bubble velocity in curvilinear coordinates
$\mathbf{F}_D, \mathbf{F}_p, \mathbf{F}_V$	Drag force, pressure force and volume force acting on a bubble
<i>Erosion risk index</i>	
Π	(Global) Erosion risk index
π_i	Panelwise erosion risk index of i -th panel
π_{ij}	Contribution to erosion risk index caused by j -th bubble
ε	Threshold pressure
B_{ij}	Filtering operator
δ	Orthogonal distance between bubble and blade surface
p^*	$= p - p_v$, pressure imbalance driving the bubble collapse
N_{bub}	Number of bubbles released during simulation
c_{vol}	Volume concentration of bubbles
S_b	Surface of the suction side
<i>Discretization</i>	
A_i	Area of i -th panel
dA_n	Area of n -th sub-panel
N_{pan}	Number of panels
N_{sub}	Number of sub-panels
r_{ij}, r_{nj}	Distance between j -th bubble and i -th panel, $\sim n$ -th and sub-panel
$\Delta t, \Delta \tilde{t}$	Time step size propeller flow simulation, \sim bubble dynamics simulation
n_{bub}	Number of bubbles released per time step Δt
<i>Propeller flow</i>	
$R, D = 2R$	Propeller radius, diameter
n_z	Number of blades
n	Rate of revolutions
r	Radial position of a blade section
V_s	Ship speed
V_a	Axial component of the inflow
V_e	$= \sqrt{V_a^2 + (2\pi nr)^2}$, total inflow velocity
$J = \frac{V}{nD}$	Advance coefficient with V being averaged axial inflow velocity

$\sigma_n = \frac{p_{\text{ref}} - p_v}{\rho/2n^2D^2}$ Cavitation number with reference velocity nD

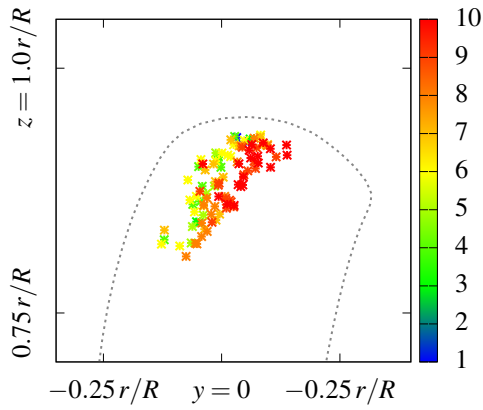
p_{ref} Reference pressure at propeller shaft

Superscripts, subscripts and operators

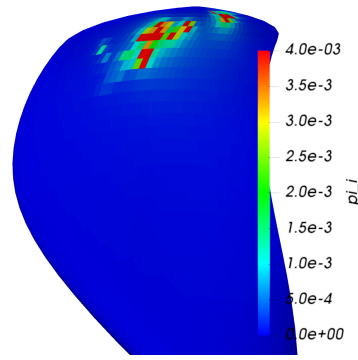
$\{\cdot\}_0$ Initial state
 $\{\cdot\}_{\text{max}}, \{\cdot\}_{\text{min}}$ Maximum, minimum of a quantity
 $\{\cdot\}_{\text{lim}}$ Threshold value
 $\{\cdot\}_{i,j,k,l}$ Running indices

REFERENCES

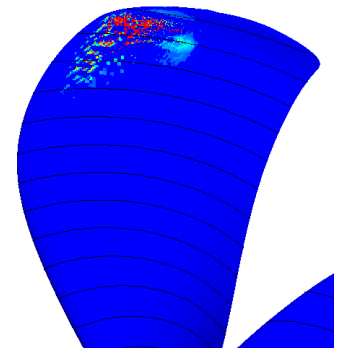
- Abdel-Maksoud, M., Hänel, D., and Lantermann, U. (2010). Modeling and computation of cavitation in vortical flow. *International Journal of Heat and Fluid Flow*, 31(6):1065–1074.
- Andersen, P., Friesch, J., Kappel, J. J., Lundegaard, L., and Patience, G. (2005). Development of a Marine Propeller With Nonplanar Lifting Surfaces. *Marine Technology*, 42(3):144–158.
- Brennen, C. E. (2002). Fission of collapsing cavitation bubbles. *Journal of Fluid Mechanics*, 472:153–166.
- Eskilsson, C. and Bensow, R. E. (2015). Estimation of Cavitation Erosion Intensity Using CFD: Numerical Comparison of Three Different Methods. In *Fourth International Symposium on Marine Propulsors*, Austin, Texas, USA.
- Franc, J. P. (2007). The Rayleigh-Plesset Equation: A Simple and Powerful Tool to Understand Various Aspects of Cavitation. In d'Agostino, L. and Salvetti, M. V., editors, *Fluid Dynamics of Cavitation and Cavitating Turbopumps*, CISM Courses and Lectures, pages 1–41. Springer.
- Franc, J. P. and Michel, J.-M. (2005a). Cavitation Erosion. In *Fundamentals of Cavitation*, chapter 12, pages 265–291. Kluwer Academic Publishers.
- Franc, J. P. and Michel, J.-M. (2005b). Further Insights into Bubble Physics. In *Fundamentals of Cavitation*, chapter 5, pages 77–96. Kluwer Academic Publishers.
- Fukaya, M., Tamura, Y., and Matsumoto, Y. (2010). Prediction of Cavitation Intensity and Erosion Area in Centrifugal Pump by Using Cavitating Flow Simulation with Bubble Flow Model. *Journal of Fluid Science and Technology*, 5(2):305–316.
- Hasuike, N., Yamasaki, S., and Ando, J. (2009). Numerical Study on Cavitation Erosion Risk of Marine Propellers Operating in Wake Flow. In *Seventh International Symposium on Cavitation*, Ann Arbor, Michigan, USA.
- Kato, H., Konno, A., Maeda, M., and Yamaguchi, H. (1996). Possibility of Quantitative Prediction of Cavitation Erosion Without Model Test. *Transactions of ASME*, 118:582–588.



(a) Bubble collapses.

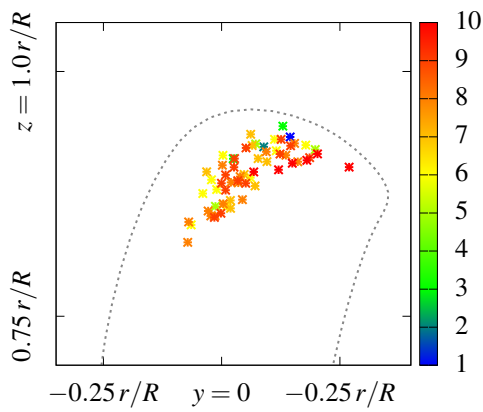


(b) Panelwise erosion risk index π_i .

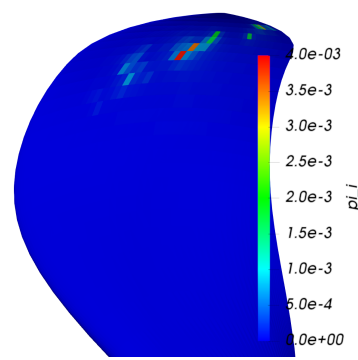


(c) Erosion risk DES analysis.

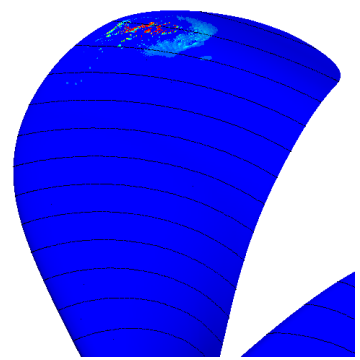
Figure 14: Erosion risk analysis Propeller P1.1.



(a) Bubble collapses.

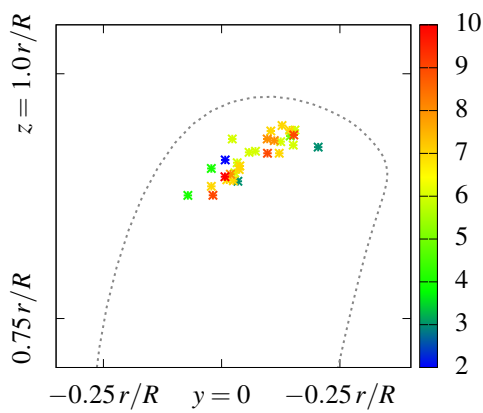


(b) Panelwise erosion risk index π_i .

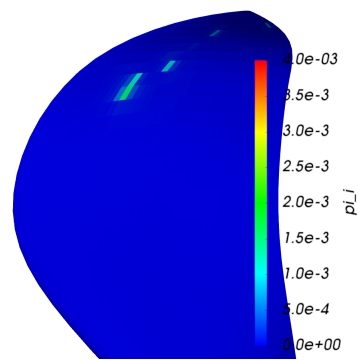


(c) Erosion risk DES analysis.

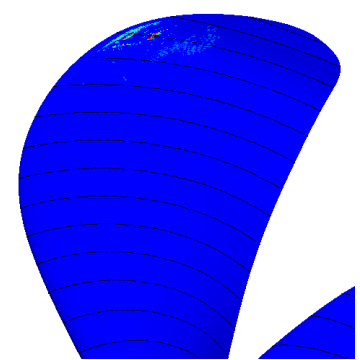
Figure 15: Erosion risk analysis Propeller P1.2.



(a) Bubble collapses.



(b) Panelwise erosion risk index π_i .



(c) Erosion risk DES analysis.

Figure 16: Erosion risk analysis Propeller P1.3.

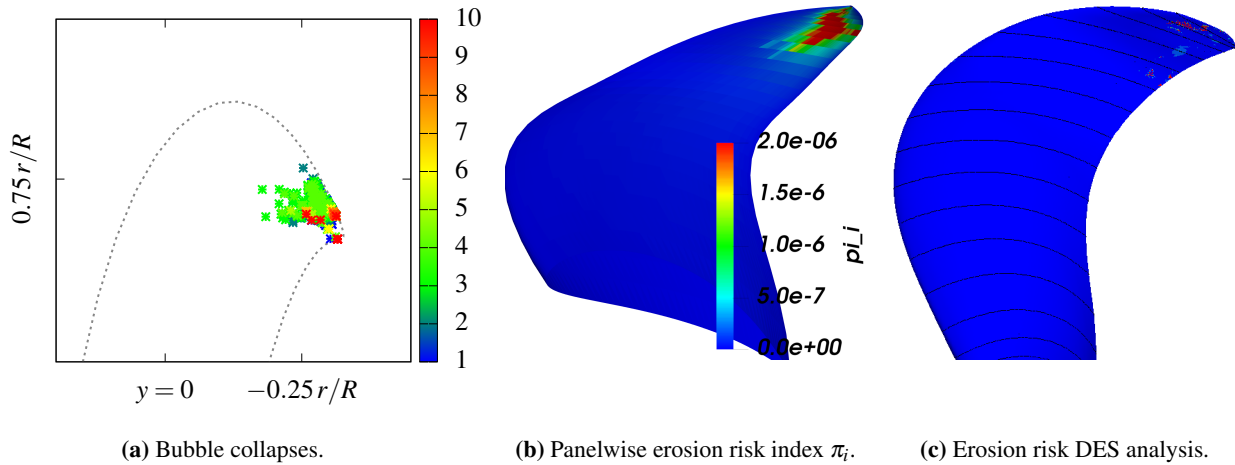


Figure 17: Erosion risk analysis Propeller P2.1.

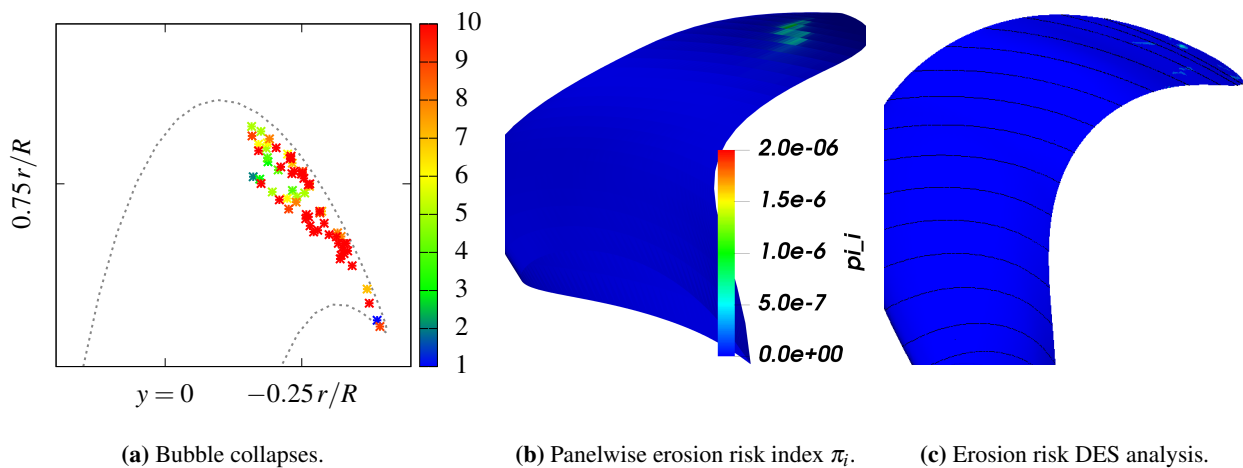


Figure 18: Erosion risk analysis Propeller P2.2.

Li, Z. and van Terwisga, T. (2012). On the Capability of a RANS Method to Assess Cavitation Erosion on a Hydrofoil. In Eighth International Symposium on Cavitation, Singapore.

Ochiai, N., Iga, Y., Nohmi, M., and Ikohagi, T. (2009). Numerical Prediction of Cavitation Erosion in Cavitating Flow. In Seventh International Symposium on Cavitation, Ann Arbor, Michigan, USA.

Okada, T., Iwai, Y., Hattori, S., and Tanimura, N. (1995). Relation between Impact Load and the Damage produced by Cavitation Bubble Collapse. Wear, 184:231–239.

Regener, P. B. (2017). Hull–Propeller Interaction and Its Effect on Propeller Cavitation. Dissertation, Technical University of Denmark, Kgs. Lyngby.

Ross, D. (1976). Mechanics of Underwater Noise. Pergamon Press, New York.

Shin, K. W. and Andersen, P. (2015). CFD Analysis of Cloud Cavitation on Three Tip-Modified Pro-

pellers with Systematically Varied Tip Geometry. In Ninth International Symposium on Cavitation, Lausanne, Switzerland.

Shin, K. W., Regener, P. B., and Andersen, P. (2015). Methods for Cavitation Prediction on Tip-Modified Propellers in Ship Wake Fields. In Fourth International Symposium on Marine Propulsors, Austin, Texas, USA.

Soyama, H., Kumano, H., and Saka, M. (2001). A New Parameter to Predict Cavitation Erosion. In Fourth International Symposium on Cavitation, Pasadena, California, USA.

Tomita, Y. and Akira, S. (1977). On the Behavior of a Spherical Bubble and the Impulse Pressure in a Viscous Compressible Liquid. Bulletin of JSME, 20(149):1453–1460.

Zhang, Y. J., Li, S. C., and Hammit, F. G. (1989). Statistical Investigation of Bubble Collapse and Cavitation Erosion Effect. Wear, 133:257–265.